Accepted Manuscript

Nanoparticles for multi-modality cancer diagnosis: Simple protocol for self-assembly of gold nanoclusters mediated by gadolinium ions

Wenxiu Hou, Fangfang Xia, Gabriel Alfranca, Hao Yan, Xiao Zhi, Yanlei Liu, Chen Peng, Chunlei Zhang, Jesus Martinez de la Fuente, Daxiang Cui

PII: S0142-9612(16)30746-3

DOI: 10.1016/j.biomaterials.2016.12.027

Reference: JBMT 17876

To appear in: *Biomaterials*

Received Date: 23 September 2016

Revised Date: 11 December 2016

Accepted Date: 24 December 2016

Please cite this article as: Hou W, Xia F, Alfranca G, Yan H, Zhi X, Liu Y, Peng C, Zhang C, de la Fuente JM, Cui D, Nanoparticles for multi-modality cancer diagnosis: Simple protocol for self-assembly of gold nanoclusters mediated by gadolinium ions, *Biomaterials* (2017), doi: 10.1016/j.biomaterials.2016.12.027.

Nanoparticles for multi-modality cancer diagnosis: Simple protocol for self-assembly of gold nanoclusters mediated by gadolinium ions

Wenxiu Hou [a,b,#], Fangfang Xia [a,#], Gabriel Alfranca[a,d], Hao Yan [a], Xiao Zhi[a], Yanlei Liu [a,b], Chen Peng[c]*, Chunlei Zhang[a]*, Jesus Martinez de la Fuente[a,d], Daxiang Cui[a]*

[a]Institute of Nano Biomedicine and Engineering, Shanghai Engineering Research Centre for Intelligent Diagnosis and Treatment Instrument, Department of Instrument Science and Engineering, School of Electronic Information and Electrical Engineering, Shanghai Jiao Tong University, 800 Dongchuan RD, Shanghai 200240, P.R. China

[b]School of Biomedical Engineering, Shanghai Jiao Tong University, 800 Dongchuan RD, Shanghai 200240, P.R. China

[c]Department of Radiology, Shanghai Tenth People's Hospital, School of Medicine, Tongji University, Shanghai, 200072, P.R. China.

[d]Instituto de Ciencia de Materiales de Aragón, Consejo Superior de Investigaciones Científicas/Universidad de Zaragoza, Spain.

[#]These authors equally contributed to this work.

* Corresponding author.

E-mail: dxcui@sjtu.edu.cn

E-mail: cpengrr@tongji.edu.cn

E-mail: chunleizhang@sjtu.edu.cn

ABSTRACT:

It is essential to develop a simple synthetic strategy to improve the quality of multifunctional contrast agents for cancer diagnosis. Herein, we report a time-saving method for gadolinium (Gd^{3+}) ions-mediated self-assembly of gold nanoclusters (GNCs) into monodisperse spherical nanoparticles (GNCNs) under mild conditions. The monodisperse, regular and colloidal stable GNCNs were formed via selectively inducing electrostatic interactions between negatively-charged carboxylic groups of gold nanoclusters and trivalent cations of gadolinium in aqueous solution. In this way, the Gd^{3+} ions were chelated into GNCNs without the use of molecular gadolinium chelates. With the co-existence of GNCs and Gd^{3+} ions, the formed GNCNs exhibit significant luminescence intensity enhancement for near-infrared fluorescence (NIRF) imaging, high X-ray attenuation for computed tomography (CT) imaging and reasonable r1 relaxivity for magnetic resonance (MR) imaging. The excellent biocompatibility of the GNCNs was proved both *in vitro* and *in vivo*. Meanwhile, the GNCNs also possess unique NIRF/CT/MR imaging ability in A549 tumor-bearing mice. In a nutshell, the simple and safe GNCNs hold great potential for tumor multi-modality clinical diagnosis.

Keywords: Gold nanoclusters (GNCs) · Gd^{3+} ions · Assembly · Multi-modality imaging · Diagnosis

1. Introduction

Nowadays, there is an increasing interest in the development of molecular imaging technology for applications in early-stage cancer imaging diagnosis[1, 2]. Among various imaging modalities, near-infrared fluorescence (NIRF)[3], computed tomography (CT)[4] and magnetic resonance (MR)[5] imaging are three of the most widely used imaging techniques for disease diagnosis. NIRF imaging possesses high sensitivity. But it cannot guarantee an adequate spatial resolution [6]. CT imaging is a time-saving and low cost imaging technique with excellent density and spatial resolution. Despite of high-resolution images of anatomic structures, CT imaging is trapped in soft-tissue imaging applications due to the inadequacy of sensitivity [4]. Besides, MR imaging is a non-invasive technique with high sensitivity, good tissue penetration depth, and detailed profile ability of soft-tissues. But it is unable to detect lesions of bone structures [7]. Due to the limitations of the individual imaging technique discussed above, the use of dual mode or multimode imaging is indispensable for comprehensive and accurate cancer diagnosis, especially for early-stage cancer diagnosis [8-10]. To present day, the development of nanoparticle-based contrast agents provide a promising way to integrate the advantages of different imaging techniques for accurate cancer diagnosis and for extending the application scope of molecular imaging[11-14]. Nevertheless, most of the contrast agents used in the clinic are only suitable for single modality imaging. Meanwhile, complicated architectures and synthetic processes are always required to synthesize multifunctional nanoparticle-based contrast agents for multi-modality cancer diagnosis [11, 15, 16]. Thus, the development of a simple and time-saving protocol to synthesize a single nanostructure bearing various contrast agents for different imaging modalities would bring a great improvement towards an accurate cancer diagnosis.

Among the numerous nanoparticles described nowadays [12, 13, 17, 18], the noble metal nanoclusters (NCs) are ultrasmall nanoparticles (with a core size smaller than 2 nm) with well-defined sizes, components and charges[19, 20]. They possess strong luminescence and enhanced catalytic activity which make them especially attractive in

biomedical areas for biosensing[21], bioimaging [22, 23], and therapy [24, 25]. Generally speaking, polymers, dendrimers, biological molecules or polyelectrolytes are the main templates used to synthesize NCs in solution [24, 26-28]. Glutathione (GSH)-capped gold nanoclusters (GNCs) are one kind of noble metal nanoclusters that are synthesized using glutathione as thiolate ligand, and can be denoted as $Au_n(SG)_m$ (where n is the number of gold atoms, and m is the number of glutathione molecules) [29-31]. The GNCs composed of a dozen to about a hundred gold atoms possess many advantages for biomedical applications, such as excellent biocompatibility, good water solubility, faster clearance by normal tissues, longer retention time in the tumor, and easily functionalized surface ligands [26, 32, 33]. Moreover, the intrinsic characteristics of GNCs, red-near-infrared fluorescence, large two-photon excitation and excellent X-ray attenuation, make them highly suitable for both *in vitro* and *in vivo* NIRF and CT imaging [29, 33-35]. Therefore, the GNCs may have a great potential for multi-modality cancer diagnosis. Nowadays, the lanthanide ion Gd^{3+} based contrast agents have been widely studied for cancer diagnosis [16, 36, 37]. But the development of sensitive, biocompatible, and stable Gd^{3+}-based contrast agents without the use of molecular gadolinium chelates still remains as an interesting approach and great challenge. Based on the qualities of GNCs and lanthanide Gd^{3+} ions, an exciting methodology for biomedical applications could be development of an effective and simple method to assemble GNCs and Gd^{3+} ions into a single multifunctional spherical nanoparticle for cancer multi-modality imaging. According to a previous report [38], the GNCs could be assembled into monodisperse and uniform spheres via selectively inducing interaction of electrons between divalent cations and negatively-charged GNCs. In this scenario, the GNCs can sever as a new family of ion mimics (‘‘nanoions’’) in aqueous solution where the self-assemble process is analogous to the theory of formation of ionic crystals from real ions. Using the above theory, the hydrophilic GNCs could be assembled into monodisperse spherical shapes via the strong interaction of electrons between negatively-charged GNCs and trivalent counter cations of gadolinium. If properly implemented, this method to combine GNCs and Gd^{3+} ions would be a simple and time-saving approach to assemble them into a single nanoparticle for multi-modality

tumor imaging.

Herein, we report the assembly of gold nanoclusters into monodisperse regular and stable spherical nanoparticles (GNCNs) by a selective electrostatic interaction for enhanced tumor multi-modality imaging (scheme 1). This simple and time-saving electrostatic interaction occurs between negatively-charged carboxylic groups on the gold nanoclusters and trivalent cations of gadolinium (Gd^{3+}) in aqueous solution under mild conditions. The assembly behavior only occurs when the ratio of Gd^{3+} ions and carboxylate groups exceeds certain threshold values. Such behavior is different from the random aggregation of colloidal nanoparticles by counter ions. With the co-existence of GNCs and Gd^{3+} ions, the formed GNCNs exhibit an enhanced fluorescence, high X-ray attenuation and reasonable r1 relaxivity. All of these properties ensure that GNCNs could be used as NIRF/CT/MR multi-modality imaging contrast agents for accurate diagnosis of different types of tumor. The physicochemical properties of the synthesized GNCNs were extensively characterized via various techniques. In addition, both *in vitro* and *in vivo* experiments are carried out to carefully evaluate the biocompatibility, cellular uptake efficacy and tumor NIRF/CT/MR multi-modality imaging performance. We believe that the multifunctional spherical GNCNs are novel, simple and safe nanoparticles, which hold great potential for cancer NIRF/CT/MR multi-modality clinical diagnose.

2. Materials and methods

2.1. Materials

Tetrabutylammonium borohydride (TBAB; 95%) and Gadolinium chloride hexahydrate ($GdCl_3 \cdot 6H_2O$) were obtained from Aladdin Reagent Co. Ltd. (Shanghai China). Sephadex G-150 was purchased from Pharmacia (Uppsala, Sweden). 3-[4,5-Dimethylthiazol-2yl]-2,5-diphenyltetrazolium bromide (MTT), Gold chloride trihydrate ($HAuCl_4 \cdot 3H_2O$, 99%) and Hoechst 33342 were received from Sigma Chemical Corporation (St Louis, USA). The reagents related to cell culture were obtained from Hyclone. Ultrapure water with resistivity of 18.2 MΩ was used in the

preparation of all aqueous solutions.

2.2. Synthesis of red-emitting GNCs

The procedure to synthesize red-emitting GNCs is similar to our previous study [24]. Briefly, the freshly prepared $HAuCl_4$ (5 mL, 0.02 M) and GSH (2 mL, 0.15 M) were diluted with 87 mL cold deionized water under vigorous stirring for 3 min. Then the mixture was added with icy cold TBAB solution (6 mL, 0.186 M) under a quickly vigorous stirring for 5 min. After the mixture was maintained for 2 h without vigorous stirring in ice bath, 1M HCl was added to adjust the pH of the reaction to about 3.0. Then the insoluble Au(I)−thiolate complex were separated by centrifugation. After another 12 h incubation of the mixture in ice bath, the supernatant was added with NaCl (to about 10×10^{-3} M) and cold methyl alcohol to collect the precipitates. The precipitates were dialyzed for three days against ultrapure water to obtain the GNCs.

2.3. Gd (III) ions-induced assembly of red-emitting GNCs

Before the reaction, the above prepared GNCs (1.25 mg/mL) and the $GdCl_3 \cdot 6H_2O$ in specific concentration were dissolved in the aqueous solution, respectively. Then the pH of the each solution was adjusted to about 6.5. The $GdCl_3$ solution was freshly prepared and sonicated for 3 min by an ultrasonicator at 100 W before used. Taking $R_{[Gd^{3+}]/[GSH]}$ =0.08 as an example, 0.25mL of 0.73 mM $GdCl_3$ aqueous solution was added dropwise into GNCs aqueous solution (1.25 mg/mL,1mL) under stirring and maintained at 30 ^oC for 3 h. The gel filtration method (Sephadex G-150 column equilibrated with the ultrapure water) was used to purify the assembled GNCs (GNCNs). Assembly of GNCs by Gd^{3+} ions in other concentration was also synthesized in the similar steps.

2.4. Characterization

The size and the morphology of GNCNs were evaluated by transmission electron microscopy (TEM), high resolution TEM (HR-TEM) and field emission scanning electron microscopy (SEM). The composition of GNCNs was measured by energy-dispersive X-ray spectroscopy (EDX) and scanning transmission electron

microscopy (STEM). PL spectra were characterized by a Hitachi FL-4600 spectrofluorometer. UV-vis spectra were tested with a Varian Cary 50 spectrophotometer (Varian Inc., USA). The size and ζ-potential of GNCNs were estimated by a Nicomp 380 ZLS Zeta potential/Particle sizer (PSS Nicomp, USA). Moreover, the aqueous solution of GNCs, GNCNs, Omnipaque and Gd-DTPA were prepared into Eppendorf tubes (1.5 mL) with different concentrations before CT or MR imaging. The dual-source CT system (SOMATOM Definition Flash, Siemens, Erlangen, Germany) was used to perform the CT scanning with the parameters set to 100 kV, 80 mA, and a slice thickness of 0.625 mm. Hounsfield units (HU) for the regions of interest were used to determine the contrast enhancement of each sample and each sample was measured for 3 times. The T1 relaxation times of the GNCNs and Gd-DTPA with different Gd^{3+} concentrations was performed using a 0.5T NMI20-Analyst NMR Analyzing and Imaging system (Shanghai Niumag Corporation, China) with 0.6 mm section thickness, TE = 160 ms, TR = 600 ms, 156 mm × 156 mm point resolution and one time excitation. The T1 relaxivity was measured by a linear fitting of the *T1* relaxation time (1/T1) as a function of the Gd^{3+} ions concentration.

2.5. Cell culture

The A549 cells (human non-small cell lung cancer cell) were chosen as modal cells in this study. DMEM medium with 10% FBS was used to incubate A549 cells at 37 °C with 5% CO_2.

2.6. Cytotoxicity and hemolysis assay

MTT assay, The A549 cells viability was tested by the MTT assay to evaluate the cytotoxicity of the GNCNs. Briefly, the cells were seeded into a 96-well plate (5×10^3 cells/well) and incubated in medium for 24 h. After that, the fresh medium containing GNCNs at different Au concentrations or PBS (control group) were used to replace the above medium, respectively. After 24 h and 48 h incubation, the medium was added with MTT (5 mg/mL, 20 mL) and maintained incubation for another 4 h, respectively. The cell viability was assessed refer to the previous report.[39]

Apoptosis assay, in briefly, A549 cells at 2.0×10^5 cells/well were seeded in 6-well plates for 24 h. Then, the cells were incubated with GNCNs at different Au concentrations or PBS (control group) for 24 h. The distributions of necrotic or apoptotic cells induced by GNCNs were measured on the basis of the manufacturer's protocol of Annexin V-FITC/PI apoptosis detection kit. The flow cytometry (BD FACSCalibur, BD Biosciences, USA) was used to measure the apoptosis of GNCNs treated cells. The data were analyzed by FlowJo 7.6 software.

Hemolysis assay, the fresh human blood was centrifuged at 1000 rpm for 10 min to remove the supernatant. Then, the blood was washed with PBS for 5 times to acquire the red blood cells (HRBCs). The HRCBCs suspension (0.1mL) was diluted into 0.9 mL PBS (negative control group), 0.9 ml water (positive control group), or 0.9 mL GNCNs PBS solution at different Au concentrations (22-550 μM), respectively. The mixtures were reacted at room temperature for 2 h, after a gentle shaking. After that, the mixtures were centrifuged at 10000 rpm for 1 min. The absorbance of the supernatants at 541nm and the photos of the mixtures were recorded to measure the hemolysis of GNCNs. The hemolysis percentages = (OD541 nm of the experiment group - OD541 nm of the negative control group)/(OD541 nm of the positive control – OD541 nm of the negative control group)×100%.

2.7. Cellular uptake assay

Confocal microscopy experiments, A549 cells (2.0×10^4 cells/well) were seeded in coverglass in 24-well plates. After 24 h incubation, the cells were co-incubation with GNCs or GNCNs at Au concentration of 550 μM for 4 h and 10 h, respectively. After two times washed with PBS, the cells were fixed by the 2.5% glutaraldehyde for 30 min at 4 °C. Then Hoechst 33342 was used to stain nuclei at room temperature for 15 min. The nuclei was detected by the blue diode 405 nm laser. And the GNCNs and GNCs were excited at 620 nm on the TCS SP8 confocal laser scanning microscope.

Flow cytometry (FCM) measurements, A549 cells (2.0×10^5 cells/well) were plated onto 6-well plates and cultured in medium for 24 h. Then, the cells were treated with GNCs or GNCNs at Au concentration of 550 μM for 4 h and 10 h, respectively. FL3

channel was used to measure the amount of GNCs or GNCNs in A549 cells, respectively.

ICP-MS measurements, similar to the steps of FCM measurements, the A549 cells were collected and then digested by aqua regia before quantifying by ICP-MS. Besides, the A549 cells were also co-incubated with GNCNs or GNCs at different Au concentrations ([Au] = 0-550μM) for 10 h to test the cell uptake efficiency by ICP-MS.

2.8. In vitro NIRF/CT/MR imaging

Approximately 2×10^6 A549 cells were seeded in 5 mL cell culture flask and then were incubated for 24 h. After that, the cells were co-incubated with 2 mL fresh medium containing GNCNs or GNCs at different Au concentrations ([Au] = 0-550 μM). After 10 h incubation, the cells were resuspended in 100 μL PBS and placed in 1.5 mL Eppendorf tubes. The *in vivo* tumor CT imaging studies were conducted with dual-source CT system. The T1-weighted MR imaging of the A549 cells incubation with the GNCNs was measured by a 3.0 T clinical MR imaging instrument (SOMATON Definition Flash, Siemens, Erlangen, Germany). MR images of A549 cells were acquired with slice thickness = 0.7 mm, TR = 280 ms, TE = 15 ms, 318×314 matrix and 80×100 FOV. The signal to noise ratio (SNR) (T1-weighted MRI signal intensity of the tumor area/T1-weighted MRI signal intensity of air area) was calculated to quantify the T1-weighted MRI effect of the GNCNs. For *in vitro* NIRF imaging, A549 cells (5×10^3 per well was pelted in 96-well plates) were incubated with GNCNs or GNCs (at the same Au concentrations for CT/MR imaging) for 10 h. Then, the Bruker In-Vivo F PRO imaging system (Billerica, USA) was used to obtain fluorescence images with excitation: 530/20 nm, emission: 700/30 nm and integration time: 20 s.

2.9. In vivo NIRF/CT/MR imaging

Female and male BALB/c-nude mice (4 weeks of age) were obtained from Shanghai Slac Laboratory Animal Co., Ltd. According to the Institutional Animal Care and Use Committee of Shanghai Jiao Tong University, all animals received care. In the right flank regions of mice, 4×10^6 A549 cells/mouse were subcutaneously injected to

establish A549 tumor model. The volume of tumors were allowed to reach ~200 mm^3 before the NIRF/CT/ MR imaging.

For the CT imaging, the mice were randomly allocated into 2 groups. Mice in group 1 were intravenously injected with GNCs. Mice in group 2 were intravenously injected with GNCNs (both containing 0.11 M Au, 150 μL per mouse). The CT scanning was executed at different time points by using a dual-source CT system. For MR imaging, the mice were given tail intravenous injection with the GNCNs ([Gd] = 5mM, 150 μL per mouse). The T1-weighted MR imaging of the mice was carried out by using a 3.0 T clinical MR imaging instrument. Moreover, at preset time points, the fluorescence images were acquired after the mice were intratumoral injected with the GNCs or GNCNs ([Au] = 0.11 M, 50 μL per mouse), by using a Bruker In-Vivo F PRO imaging system (Billerica, USA). The mice were sacrificed and the tumors and main organs were extracted for *ex vivo* NIRF imaging at 24 h post-injection,. The Bruker Molecular Imaging Software 7.1 Version was used to quantify the average fluorescence intensity of the excised organs and tumor.

2.10. In vivo biodistribution of GNCNs

For *in vivo* biodistribution studies of GNCNs, the A549 tumor bearing mice were caudal vein injected with GNCNs ([Au] = 0.11 M, 150 μL per mouse). After 20 min, 60 min and 6 h post injection, the mice were sacrificed and the main organs (heart, spleen, lung, kidney, and liver), blood and tumors were extracted and weighed, respectively. The gold and gadolinium elements content in organs, blood and tumors were analyzed by ICP-OES, after digesting the extracted samples in aqua regia solution overnight.

2.11. In vivo security evaluation

Blood analysis, the BALB/c female mice were intravenously injected with GNCNs ([Au] = 0.11 M, 300 μL per mouse). The weight was measured for 21 days after intravenous injection. 500 μL of blood was collected and separated before and after 7 days and 21 days of intravenous injection, respectively. The indicators of kidney function (creatinine (CREA), urea nitrogen (BUN) and uric acid (UA)) and liver

function (lactate dehydrogenase (LDH), alkaline phosphatase (ALP), gamma glutamyl transferase (GGT), total bilirubin (TBIL) and aspartate aminotransferase (AST)) were tested by standard biochemical examination.

For the histochemical analysis, the main organs (liver, lung, spleen, heart, and kidney) were harvested before and after 21 days of tail intravenous injection of GNCNs. Then hematoxylin and eosin (HE) staining assay were performed to detect the change in morphological features of each organ.

2.12. Statistical analysis

All data were expressed as mean ± SD (Standard Deviation) of at least three independent experiments unless otherwise specified.

3. Results and discussions

3.1. Synthesis and characterization of GNCs and GNCNs

The TBAB-reduction method [24, 40] was used to synthesize red-emitting and glutathione (GSH)-capped gold nanoclusters (GNCs), with a main fluorescence peak at 652 nm. The monodispersed spherical GNCs (with a GSH-to-Au atom ratio of 0.82) had a diameter of about 2.0 nm (Fig. S1A) and also possessed high GSH content on their surface [24, 29]. It has been reported that the pKa of the glutathione (GSH) moiety was below 4 [41]. Following this statement, all of the surface carboxylic groups would be deprotonated under neutral conditions leading to the GNCs to acquire a negative charged surface [38]. Thus, the positively charged Gd^{3+} ions could bind to the negatively charged GNCs by both strong electrostatic interactions and coordination effects, in aqueous solution [22, 42].

Gd^{3+} ions in aqueous solution were added dropwise to the aqueous solution of GNCs in different concentrations to obtain assembled GNCs (GNCNs). The morphology and size of the GNCNs were characterized by TEM. Since the Gd^{3+} ions were electrostatically bound to the carboxyl groups of the GSH on the surface of the GNCs, the size and morphology of the assembled GNCs would depend on the molar

ratio of Gd^{3+} ions to GSH (designated as $R_{[Gd^{3+}]/[GSH]}$). As shown in the inset in Fig. S1A, when no Gd^{3+} ions were added ($R_{[Gd^{3+}]/[GSH]}$ = 0), the monodispersed GNCs with spherical shape gave a brownish color to the solution and revealed a good dispersion in aqueous solution. If the $R_{[Gd^{3+}]/[GSH]}$ was increased to 0.05, the Gd^{3+} ions began to induce the assembly of the GNCs. Under these conditions, partially assembled GNCs with small spherical shapes appeared in the TEM images (Fig. S1B). Meanwhile, the status of the assembled GNCs solution displayed no visible change (inset in Fig. S1B), compared with that of the free GNCs. This may be attributed to a lack of Gd^{3+} ions, which act as the bridge to induce the assembly of GNCs [38]. Uniformed and monodispersed spherical assembled GNCs were observed in TEM images when $R_{[Gd^{3+}]/[GSH]}$ was increased to 0.08 (Fig. S1C). Under these conditions, the solution containing the assembled GNCs revealed a translucent light fawn color and showed excellent water solubility (insets in Fig. S1C). At a $R_{[Gd^{3+}]/[GSH]}$ value of 0.11, an aggregation generated from irregularly assembled structures appeared in the TEM images (Fig. S1D). The aqueous solution of the assembled GNCs became turbid and showed tawny color, which confirmed that the aggregations were successfully generated (inset in Fig. S1D). The occurrence of the aggregation was formed by bridging the individual GNCNs together under the condition of excessive Gd^{3+} ions. The size of the assembled GNCs increase with the $R_{[Gd^{3+}]/[GSH]}$ value was corroborated by the enhancement of the absorbance value observed by UV-Vis spectroscopy (Fig. S2A) [43]. The two main effects of the counter cations influencing on the assembly of GNCs have been recently reported by Yao *et al.*[38] and can be summed up as decrease in the negative charge on the GNCs and the subsequent bridging of the GNCs. This explanation matches with the increase in the zeta potential of the aqueous solution of GNCNs (pH≈6.5) with the concentration of Gd^{3+} ions (Fig. S2B). As a consequence, the GNCs were assembled at an optimal $R_{[Gd^{3+}]/[GSH]}$ value of 0.08 for their future application in tumor diagnosis.

The morphology and composition of assembled GNCs at $R_{[Gd^{3+}]/[GSH]}$ of 0.08 were also tested by HR-TEM. As shown in Fig. 1A and B, the diameter of GNCs was about 2 nm and they could be plain visualized inside the assembled GNCNs. The SEM images

with the corresponding results indicated that the GNCNs were almost uniform spheres with good monodipersity (Fig. 1C and Fig. S3). The narrow hydrodynamic diameter distribution around 200 nm of the GNCNs in aqueous solution measured by DLS (Fig. 1D) not only confirmed the results of TEM and SEM but also indicated that the GNCNs may preferentially enter the tumor tissue by the Enhanced Permeability and Retention (EPR) effect [44]. As previously reported, the ultrasmall metal GNCNs can be considered as a new family of ion mimics (‘‘nanoions’’) [38]. The high order of regularity of the assembled GNCs may be due to the selectively induced electrostatic interactions in the assembly of the GNCs, which is similar to the formation of ionic crystals from real ions while different from the random aggregation of counter ions-mediated nanoparticles [38]. Moreover, elemental line-scanning EDX and mapping EDX analysis were performed to further demonstrate the chemical composition and the atomic distribution of the GNCNs [45, 46]. Fig. 2A showed a linear distribution of elemental Au and Gd across the diameter of a typical assembly, where the concentration of Au was clearly higher than that of the Gd in the entire region of the GNCNs. In order to further research the elemental spatial distribution of Au and Gd in GNCNs, elemental mapping of EDX analysis was carried out throughout a representative sample of GNCNs, as depicted in Fig. 2A. The two recognizable signals of elemental Au and Gd were distributed uniformly in the whole volume of GNCNs, as shown in Fig. 2B-D. By combining these data with EDX spectrum analysis (Fig. 2E), the exact composition of the spherical assembly was determined. We can infer that the GNCNs were indeed formed by the assimilation of GNCs with Gd^{3+} ions. The fluorescence excitation of the GNCs and GNCNs were depicted in Fig. S4 and Fig. 3A. The addition of Gd^{3+} ions had a strong effect on the physical and chemical properties of the GNCs with an enhancement in the optical luminescence accompanied by a blue shift of the emission peak. The fluorescence intensity of GNCNs at an optimal $R_{[Gd^{3+}]/[GSH]}$ of 0.08 was almost 1-fold enhanced when compared with that of the GNCs (Fig. 3A). The increase of the optical luminescence of the GNCNs may be caused by the significantly shortened distance between the GNCs after their assembly, sequentially increasing the *inter-cluster* aurophilic interaction [47, 48] and reducing the non-irradiative relaxation

of excited electrons [48, 49]. In contrast, the fluorescence intensity was decreased at a higher $R_{[Gd^{3+}]/[GSH]}$ value of 0.11, which may be due to the sedimentation of aggregated nanoparticles [22].

3.2. Stability, cytotoxicity and hemolysis assay of the GNCNs

It is crucial to test the stability of GNCNs before they are used in biomedical applications. Herein, the stability of the nanoparticles was further confirmed by TEM, UV-Vis, and DLS. The hydrodynamic diameter of the GNCNs revealed minor fluctuations within a period of one month, suggesting that the GNCNs have a good colloidal stability and can be stored in aqueous solution without noteworthy disaggregation or aggregation for a relatively long period of time (Fig. 3B). As shown in Fig. S5A, with the exception of a slight change in the smoothness of the surface, there was no observable agglomeration or disaggregation of GNCNs in the TEM images after being stored in aqueous solution for one month, which visually confirmed the stability of the GNCNs. Furthermore, the absorption features of the UV-Vis spectra of GNCNs at different temperatures in aqueous media solution showed no detectable variation (Fig. S5B), indicating that the GNCNs nanoprobes are stable in a temperature range of 4-50 °C [50, 51]. Finally, no clear precipitation or state change were observed in the GNCNs solution after being exposed to PBS (pH=7.4) for two weeks (Fig. S5C). Although the results of Z-potential of the GNCNs in aqueous solution was very low, the observed stability of the GNCNs may be due to the surface glutathione endowing the GNCNs with a high steric hindrance. These results proved that GNCNs are stable, which is a basic feature for their future application on the biomedical field.

The cytocompatibility of the GNCNs is also a crucial indicator to test their potential for biomedical imaging applications. The cell viability was evaluated by MTT assay to assess the cytocompatibility of the GNCNs (Fig. 4A). In comparison with the control cells incubated with PBS, the viability of A549 cells had no appreciable change after 24 h treatment with the GNCNs in a concentration range of 0-550 μM of Au. After incubation with the GNCNs for 48 h, the GNCNs start to display a slight cytotoxicity at Au concentrations higher than 220 μM. The MTT results inferred that the GNCNs were

cytocompatible at the studied concentration. Moreover, the apoptosis assay of A549 cells exposed to GNCNs at different Au concentrations was measured by flow cytometry, revealing similar results to those of the MTT assay, as shown in Fig. S6.

Hemocompatibility is an important issue in blood-contacting applications of nanoparticles. Hemolysis assays were performed to examine the hemocompatibility of the GNCNs before their use as contrast agents for tumor multi-modality imaging, *in vivo* (Fig. 4B). The absorbance at 541 nm of the supernatant in the UV-Vis spectra was measured to quantify the hemolysis percentages of the GNCNs at different Au concentrations (0–550 μM). The GNCNs do not show obvious hemolytic effects at the measured Au concentrations, when compared with the positive control. The results showed that even at the maximum concentration of element Au, the hemolysis percentage of GNCNs is less than the threshold value of 5% with the highest hemolysis percentage reaching 3.15%, suggesting an excellent hemocompatibility in the studied concentration range and enabling the GNCNs to be used for future *in vivo* tumor multi-modality imaging.

3.3. T1 MR relaxometry and X-ray attenuation

With the co-existence of GNCs and Gd^{3+} ions, the formed GNCNs possess X-ray attenuation and T1 MR relaxivity properties for CT and MR imaging applications, respectively. Herein, the X-ray attenuation property and T1 MR relaxometry of the GNCNs were measured prior to *in vivo* multi-modality imaging studies. The brightness change in the CT images of GNCs, GNCNs and Omnipaque (iodine-based CT contrast agent) in various concentrations of Au or iodine revealed that the CT contrast enhancement was improved with the increase of Au or iodine concentrations (Fig. 5A). It was obvious that the brightness of the CT images and the attenuation intensity of GNCNs were higher than that of free GNCs at the same Au concentrations (Fig. 5B). That may be caused by the existence of Gd^{3+} ions, which probably contribute to a small contrast enhancement of the CT images of GNCNs [52, 53]. Compared with the Omnipaque, the enhanced X-ray attenuation property of GNCNs and GNCs may be caused by the X-ray absorption coefficient of Au is higher than that of I [4]. In addition,

with the increase of the concentration of Gd^{3+} ions, a concentration-dependent signal enhancement appeared in the T1-weighted MR images of DTPA-Gd and GNCNs (Fig. 5C). It was clear that the signal enhancement intensity of the GNCNs was better than that of the T1 contrast agent Magnevist (DTPA-Gd) at the same Gd^{3+} ions concentration. Simultaneously, the transverse relaxivity (r1) value of GNCNs was 24.64 mM^{-1} S^{-1}, which was about 4.3 times higher than that of the Magnevist (4.68 mM^{-1} S^{-1}), implying a superior contrasting ability of GNCNs in T1-weighted MRI (Fig. 5D). In the GNCNs system, compared with that of the gadolinium chelated in Magnevist, the local concentration of Gd^{3+} ions was increased and the tumbling and rotational rate of Gd^{3+} ions was reduced, which may give a higher relaxivity value to GNCNs than that of the Magnevist [9, 36, 54, 55]. In a word, the GNCNs possess an enhanced fluorescence, reasonable T1 relaxivity and highly X-ray attenuation. These properties enable them to act as a new candidate for NIRF/CT/MR imaging applications.

3.4. In vitro cellular uptake

The cellular internalization of GNCNs and GNCs in A549 cells was quantified and visually analyzed by flow cytometry (FCM) and confocal laser scanning microscopy (CLSM), respectively (Fig.6). As shown in Fig. 6A, blue fluorescence was used to localize the cell nuclei using Hoechst 33342 dye, while the GNCNs and GNCs were detected by their intrinsic red fluorescence. Similarly to the behaviors of GNCs, the GNCNs were mainly accumulated in the cytoplasm after endocytosis [24]. The efficiency of the uptake of the GNCNs and GNCs in A549 cells was clearly increased with a prolonged incubation time. For the GNCs, only a slight red fluorescence was detected, after 4 h of incubation with the A549 cells, implying that a small quantity of GNCs were internalized into the cells. On the other hand, a relatively strong red fluorescence already appeared in the cytoplasm after the A549 cells were treated with the GNCNs for 4 h. This phenomena was confirmed by the results of FCM (Fig.6B and Fig.6C), where the mean fluorescence intensity of the A549 cells treated with the GNCNs was 2.9 times higher than that of the GNCs incubated groups (Fig.6B). When the incubation time was prolonged to a total of 10 h, the amount of internalized GNCs

slightly increased. Under the physiological pH range, the surface zwitterionization of the GNCs may reduce the cellular affinity of GNCs, which may be the cause of the lower efficiency in the cellular uptake [29, 56]. In contrast, a remarkable increase of red fluorescence was detected in the cytoplasm of A549 cells after prolonging the incubation time with GNCNs to 10 h, which indicated a clear uptake enhancement of GNCNs compared with GNCs. One explanation of the increase in the cellular uptake of GNCNs may be due to the changes in their surface upon addition of Gd^{3+} ions. In this way, the linkage of the negatively charged carboxylic groups to the Gd^{3+} ions may induce the nanoparticles to change from a zwitterionic to a non-zwiterionic surface and also change their surface charge [57, 58]. Additionally, the mean fluorescence of the cells treated with GNCNs measured by FCM was approximately 5.1-fold higher than the corresponding cells incubated with GNCs, after being incubated for 10 hours (Fig.6B). Overall, the results of CLSM were consistent with those obtained by FCM, which suggested that the assembled GNCNs would improve the cell internalization of GNCs. More importantly, ICP-MS analysis was also carried out to quantify the intracellular content element of Au in A549 cells treated with GNCNs or GNCs after 4 h and 10 h of treatment, respectively. The results further proved that the GNCNs exhibited an excellent cellular uptake efficiency, compared to GNCs (Fig. S7).

3.5. In vitro multi-modality imaging of cancer cells

The multi-modality imaging ability of GNCNs was also explored in this study using A549 cancer cells. The cells were cultivated with GNCs or GNCNs at different Au or Gd^{3+} ion concentrations for 10 h before performing the multi-modality imaging. Their CT/MR/NIRF imaging capabilities were quantified by measuring the CT value, signal to noise ratio (SNR) and average fluorescence intensity, respectively. For the T1-weighted MRI, an obvious increase was observed in both the brightness and the signal to noise ratio (SNR) of T1-weighted cells MR images of GNCNs with the increase of the Gd^{3+} ions concentration (Fig. S8A and S8B), which were remarkably higher than those of PBS-incubated controls. Similarly to the T1-weighted MRI, the NIRF imaging ability of GNCNs or GNCs depends on the concentration of Au (Fig.

S9A). The average fluorescence intensity of the cells treated with GNCNs was higher than that of GNCs treated groups at the same Au concentrations, suggesting that the GNCNs were easier to uptake by A549 cells than that of GNCs (Fig. S9B). Unlike with MR and NIRF images of GNCNs treated cells, the brightness difference of the CT images of the cells treated with GNCNs or GNCs was not easily distinguishable by naked eye at various of Au concentrations (Fig. S8C) [8, 18]. Therefore, the CT values of the GNCs and GNCNs treated cells were measured with the manufacture's standard display program to detect the cells CT imaging effect of GNCs and GNCNs. As shown in Fig. S8D, the CT values of cells treated with either GNCNs or GNCs increased with the Au concentrations. A higher CT value was observed in the GNCNs treated cells than in the GNCs treated ones, confirming the enhancement of the cells uptake efficiency and the high X-ray attenuation property of GNCNs. The above conclusions were verified by ICP-MS results, in which the Au content in A549 cells treated with GNCNs was higher than that of GNCs at different Au concentrations after 10 h incubation (Fig. S10A).

3.6. In vivo tumor multi-modality imaging

To explore the possibility of GNCNs as an imaging contrast agent for clinical cancer diagnosis, the potential performance of GNCNs for multi-modality imaging was carefully evaluated by applying MR/CT/NIRF imaging techniques in mouse models with A549 xenografted tumor. For T1-weighted MRI, Fig. 7A showed that the brightness of the tumor areas remarkably heightened after injection of GNCNs. The quantified T1-weighted MRI signal intensity based on signal to noise ratio (SNR) approximately increased one time at 20 min post-injection in the tumor area, and the higher MRI signal lasted for 60 min (Fig. 7B). These observations suggested that the GNCNs can rapidly accumulate in the tumor area thanks to the passive EPR effect [59]. Thus, there is no remarkable influence on the application of the GNCNs for multi-modality cancer diagnosis, even if the selectivity of GNCNs towards cancer cells was low (Fig S10B). Meanwhile, CT imaging of the tumor area exhibited a remarkable contrast enhancement as well as T1-weighted MRI results after intravenous injection of

GNCNs or GNCs, which would be attributed to entire diffusion of the nanoparticles in the tumor via EPR effect (Fig. 7C and Fig. S11). Moreover, the CT value of the tumor area also reached a maximum at 20 min post-injection. Nevertheless, the CT value of the tumor area was higher with GNCNs than with GNCs at the same time points, inferring that the GNCNs possess a better CT imaging ability than GNCs *in vivo* (Fig. 7D).

By utilizing the intrinsic red-emitting ability of the GNCs under laser irradiation, the GNCNs and the GNCs were used in NIRF imaging applications. After intratumoral injection, the amounts of GNCNs or GNCs accumulated in the tumor areas were tested by analyzing the fluorescence signal intensity distribution around the tumors (Fig. 8A and B). The enhanced signal and intensity around the tumors of GNCNs treated mice post-injection (0 h) may be attributed to the high luminescence intensity of GNCNs, which was higher than that of free GNCs at the same Au concentrations. Moreover, the reduction of the fluorescence signal intensity around the tumor at 2, 6, 12 and 24 hours post-injection was much slower in the case of the mice injected with GNCNs than the corresponding results of the GNCs. These observations confirmed the results of CT/MR imaging, further suggesting that the assembly of GNCNs possess tumor longer retention times than that of GNCs by the passive targeting of EPR effect. Moreover, *ex vivo* NIRF imaging (Fig. 8C and D) results indicated that most of the GNCNs were accumulated in the tumor, followed by liver, kidney and lung, 24 h after intratumoral injection of GNCNs. Meanwhile, the averaged fluorescence intensity of the GNCNs in the tumor sites was much higher than that of free GNCs. To sum up, the inescapable conclusion is that the prepared GNCNs have a great potential as multifunction contrast agent for clinical cancer MR/ CT /NIRF imaging.

The biodistribution of GNCNs based on ICP-MS (Fig. S12) revealed that the elemental distribution of Au in the different organs was similar to that of Gd^{3+} ions in the mice post-injection of GNCNs, further suggesting that the GNCNs were formed by the assimilation of GNCs with Gd^{3+} ions rather than as a result of a mixture of the GNCs and Gd^{3+} ions. The ICP-MS results also indicated a fast urine elimination of GNCNs, as the GNCNs were significantly accumulated in the kidney post-injection and

were almost cleared from the kidney with a prolonged circulation time of 6 h. Future study is needed to improve the surface modification of the GNCNs aiming to increase their blood circulation time. Moreover, a small amount of Au and Gd remained in heart, liver, spleen, and lung post-injection, suggesting a low uptake of the GNCNs by the Reticulo-Endothelial System (RES) tissues and that the GNCNs were not significantly retained in the lung [54]. These observations indicated that the GNGNs are safe for *in vivo* biomedical imaging applications.

3.7. In vivo security evaluation

The *in vivo* security evaluation of imaging contrast agents is crucial for their use in clinical disease diagnosis. In this study, the body weight change, blood biochemistry analysis and HE-stained histology were performed to assess the *in vivo* safety of the GNCNs as contrast agents for multi-modality imaging. The HE stained slices of main organs (e.g., lung, heart, liver, spleen and kidney) showed no noticeable abnormality or lesion after 21 days post-injection of GNCNs (Fig. S13). The weight change is one of the main indicators of organism intoxication [39]. As shown in Fig. S14, no significant body weight loss was detected in the GNCNs treated mice and there was no death of mice in the whole time period of the experiment. Moreover, to further verify whether the GNCNs would cause damage of the liver and kidney, where the most of exogenous substances are metabolized and cleared, a blood biochemistry of main liver and kidney indicators was analyzed 7 and 21 days after intravenously injection of GNCNs. As shown in Fig. S15, neither the liver function indicators nor the kidney function revealed any significant toxicity symptoms in the GNCNs injected groups compared to that of the normal control groups [40]. All of the abovementioned data demonstrated that the GNCNs would not induce any injury to the organs and that they can be safely applied in clinic cancer imaging as contrast agents.

4. Conclusion

In this study, the gold nanoclusters (GNCs) were assembled into monodisperse spherical particles (GNCNs) in aqueous solution for enhanced tumor multi-modality

imaging by selectively inducing electrostatic interactions between trivalent cations of gadolinium and negatively-charged carboxyl groups on the GNCs. By this simple, time-saving assembly approach, the Gd^{3+} ions can be chelated into the GNCNs without using molecular gadolinium chelates, giving GNCNs regular morphology and enhanced photoluminescence properties under mild conditions. Compared with free GNCs, the resulting GNCNs have good biocompatibility both *in vitro* and *in vivo* and can be easily internalized by the A549 cells. With the co-existence of GNCs and Gd^{3+} ions, the GNCNs could be used as a multifunctional nanoplatform for NIRF/CT/MR imaging of A549 cancer cells *in vitro* and of xenografted A549 tumor models *in vivo*. Therefore, the multifunctional GNCNs hold great promise in clinic cancer diagnosis. In addition, this study may provide some guidelines for the assembly of other hydrophilic ultrasmall nanoparticles modified with carboxyl-containing surfaces, such as carbon dots and quantum dots. Such guidelines have the potential to broaden the application of these ultrasmall nanoparticles in cancer diagnosis.

Supporting Information

Supporting Information is available from the Wiley Online Library or from the author.

Acknowledgments

This work is supported by the National Key Basic Research Program (973 Project) (Project No. 2015CB931802), the National Natural Scientific Foundation of China (Grant Nos. 81401458, 81225010, 81028009, and 31170961), the 863 project of China (Project No. 2014AA020701), and the Shanghai Science and Technology Fund (Grant Nos. 14ZR1432400 and 13NM1401500).

References

[1] Sandu N, Pöpperl G, Toubert M-E, Spiriev T, Arasho B, Orabi M, et al. Current molecular imaging of spinal tumors in clinical practice. Mol Med 2011;17:308-16.

[2] Zhang J, Li C, Zhang X, Huo S, Jin S, An F-F, et al. In vivo tumor-targeted dual-modal fluorescence/CT imaging using a nanoprobe co-loaded with an aggregation-induced emission dye and gold nanoparticles. Biomaterials. 2015;42:103-11.

[3] Guo W, Sun X, Jacobson O, Yan X, Min K, Srivatsan A, et al. Intrinsically radioactive [64Cu] CuInS/ZnS quantum dots for PET and optical imaging: improved radiochemical stability and controllable cerenkov luminescence. ACS nano. 2015;9:488-95.

[4] Peng C, Qin J, Zhou B, Chen Q, Shen M, Zhu M, et al. Targeted tumor CT imaging using folic acid-modified PEGylated dendrimer-entrapped gold nanoparticles. Polym Chem. 2013;4:4412-24.

[5] Wen S, Zhao Q, An X, Zhu J, Hou W, Li K, et al. Multifunctional PEGylated Multiwalled Carbon Nanotubes for Enhanced Blood Pool and Tumor MR Imaging. Adv Healthcare Mater. 2014;3:1568-77.

[6] Smith AM, Nie S. Next-generation quantum dots. Nat Biotechnol. 2009;27:732-33.

[7] Lee J-H, Huh Y-M, Jun Y-w, Seo J-w, Jang J-t, Song H-T, et al. Artificially engineered magnetic nanoparticles for ultra-sensitive molecular imaging. Nat Med. 2007;13:95-9.

[8] Chen Q, Li K, Wen S, Liu H, Peng C, Cai H, et al. Targeted CT/MR dual mode imaging of tumors using multifunctional dendrimer-entrapped gold nanoparticles. Biomaterials. 2013;34:5200-9.

[9] Gong H, Dong Z, Liu Y, Yin S, Cheng L, Xi W, et al. Engineering of Multifunctional Nano‐Micelles for Combined Photothermal and Photodynamic Therapy Under the Guidance of Multimodal Imaging. Adv Funct Mater. 2014;24:6492-502.

[10] Wu Y, Sun Y, Zhu X, Liu Q, Cao T, Peng J, et al. Lanthanide-based nanocrystals as dual-modal probes for SPECT and X-ray CT imaging. Biomaterials. 2014;35:4699-705.

[11] Wen S, Li K, Cai H, Chen Q, Shen M, Huang Y, et al. Multifunctional dendrimer-entrapped gold nanoparticles for dual mode CT/MR imaging applications. Biomaterials. 2013;34:1570-80.

[12] Petersen AL, Henriksen JR, Binderup T, Elema DR, Rasmussen PH, Hag AM, et al. In vivo evaluation of PEGylated 64Cu-liposomes with theranostic and radiotherapeutic potential using micro PET/CT. Eur J Nucl Med Mol Imaging. 2016;43:941-52.

[13] Tian G, Zheng X, Zhang X, Yin W, Yu J, Wang D, et al. TPGS-stabilized NaYbF 4: Er upconversion nanoparticles for dual-modal fluorescent/CT imaging and anticancer drug delivery to overcome multi-drug resistance. Biomaterials. 2015;40:107-16.

[14] Zhao L, Wen S, Shi X, Zhao J. 99mTc labeled multifunctional polyethylenimine-entrapped gold nanoparticles for dual mode SPECT and CT imaging. J Nucl Med. 2016;57:1091-91.

[15] Zhou C, Hao GY, Thomas P, Liu JB, Yu MX, Sun SS, et al. Near-Infrared Emitting Radioactive Gold Nanoparticles with Molecular Pharmacokinetics. Angew Chem-Int Edit. 2012;51:10118-22.

[16] Hu D-H, Sheng Z-H, Zhang P-F, Yang D-Z, Liu S-H, Gong P, et al. Hybrid gold–gadolinium nanoclusters for tumor-targeted NIRF/CT/MRI triple-modal imaging in vivo. Nanoscale. 2013;5:1624-8.

[17] Ye E, Win KY, Tan HR, Lin M, Teng CP, Mlayah A, et al. Plasmonic Gold Nanocrosses with Multidirectional Excitation and Strong Photothermal Effect. J Am Chem Soc. 2011;133:8506-9.

[18] Li J, Hu Y, Yang J, Wei P, Sun W, Shen M, et al. Hyaluronic acid-modified Fe 3 O 4@ Au core/shell nanostars for multimodal imaging and photothermal therapy of tumors. Biomaterials. 2015;38:10-21.

[19] Chen Y-S, Choi H, Kamat PV. Metal-cluster-sensitized solar cells. A new class of thiolated gold sensitizers

delivering efficiency greater than 2%. J Am Chem Soc. 2013;135:8822-5.

[20] Zhu Y, Qian H, Zhu M, Jin R. Thiolate‐Protected Aun Nanoclusters as Catalysts for Selective Oxidation and Hydrogenation Processes. Adv Mater. 2010;22:1915-20.

[21] Chen L-Y, Wang C-W, Yuan Z, Chang H-T. Fluorescent gold nanoclusters: recent advances in sensing and imaging. Anal Chem. 2014;87:216-29.

[22] Yahia-Ammar A, Sierra D, Mérola F, Hildebrandt N, Le Guével X. Self-Assembled Gold Nanoclusters for Bright Fluorescence Imaging and Enhanced Drug Delivery. ACS nano. 2016;10:2591-9.

[23] Le Guével X. Recent advances on the synthesis of metal quantum nanoclusters and their application for bioimaging. IEEE J Sel Top Quantum Electron. 2014;20:6801-12.

[24] Zhang C, Li C, Liu Y, Zhang J, Bao C, Liang S, et al. Gold Nanoclusters‐Based Nanoprobes for Simultaneous Fluorescence Imaging and Targeted Photodynamic Therapy with Superior Penetration and Retention Behavior in Tumors. Adv Funct Mater. 2015;25:1314-25.

[25] Fernández TD, Pearson JR, Leal MP, Torres MJ, Blanca M, Mayorga C, et al. Intracellular accumulation and immunological properties of fluorescent gold nanoclusters in human dendritic cells. Biomaterials. 2015;43:1-12.

[26] Zheng J, Zhou C, Yu M, Liu J. Different sized luminescent gold nanoparticles. Nanoscale. 2012;4:4073-83.

[27] Xie J, Zheng Y, Ying JY. Protein-directed synthesis of highly fluorescent gold nanoclusters. J Am Chem Soc. 2009;131:888-9.

[28] Shen Z, Duan H, Frey H. Water‐soluble fluorescent Ag nanoclusters obtained from multiarm star poly (acrylic acid) as “molecular hydrogel” templates. Adv Mater. 2007;19:349-52.

[29] Zhang C, Zhou Z, Qian Q, Gao G, Li C, Feng L, et al. Glutathione-capped fluorescent gold nanoclusters for dual-modal fluorescence/X-ray computed tomography imaging. J Mater Chem B. 2013;1:5045-53.

[30] Wu Z, Jin R. Stability of the Two Au− S Binding Modes in Au25 (SG) 18 Nanoclusters Probed by NMR and Optical Spectroscopy. ACS nano. 2009;3:2036-42.

[31] Guan G, Low M, Liu S, Cai Y, Zhang S, Geng D, et al. Destabilization of Thiolated Gold Clusters for the Growth of Single‐Crystalline Gold Nanoparticles and Their Self‐Assembly for SERS Detection. Part Part Syst Charact. 2015;32:588-95.

[32] Zhu M, Qian H, Jin R. Thiolate-protected Au20 clusters with a large energy gap of 2.1 eV. J Am Chem Soc. 2009;131:7220-1.

[33] Zhang XD, Chen J, Luo Z, Wu D, Shen X, Song SS, et al. Enhanced Tumor Accumulation of Sub‐2 nm Gold Nanoclusters for Cancer Radiation Therapy. Adv Healthcare Mater. 2014;3:133-41.

[34] Aldeek F, Muhammed MH, Palui G, Zhan N, Mattoussi H. Growth of highly fluorescent polyethylene glycol-and zwitterion-functionalized gold nanoclusters. ACS nano. 2013;7:2509-21.

[35] Shang L, Stockmar F, Azadfar N, Nienhaus GU. Intracellular thermometry by using fluorescent gold nanoclusters. Angew Chem-Int Edit. 2013;52:11154-7.

[36] Song X, Liang C, Gong H, Chen Q, Wang C, Liu Z. Photosensitizer‐Conjugated Albumin− Polypyrrole Nanoparticles for Imaging‐Guided In Vivo Photodynamic/Photothermal Therapy. Small. 2015;11:3932-41.

[37] Zhou J, Lu Z, Shan G, Wang S, Liao Y. Gadolinium complex and phosphorescent probe-modified NaDyF 4 nanorods for T 1-and T 2-weighted MRI/CT/phosphorescence multimodality imaging. Biomaterials. 2014;35:368-77.

[38] Yao Q, Luo Z, Yuan X, Yu Y, Zhang C, Xie J, et al. Assembly of nanoions via electrostatic interactions: ion-like behavior of charged noble metal nanoclusters. Sci Rep. 2014;4:3848.

[39] Hou W, Xia F, Alves CS, Qian X, Yang Y, Cui D. MMP2-targeting and redox-responsive PEGylated chlorin e6 nanoparticles for cancer near-infrared imaging and photodynamic therapy. ACS Appl Mater Interfaces. 2016;8:1447-57.

[40] Zhang C, Zhou Z, Zhi X, Ma Y, Wang K, Wang Y, et al. Insights into the distinguishing stress-induced cytotoxicity of chiral gold nanoclusters and the relationship with GSTP1. Theranostics. 2015;5:134-149.

[41] Pirie NW, Pinhey KG. The titration curve of glutathione. J Biol Chem. 1929;84:321-33.

[42] Ye D-X, Ma Y-Y, Zhao W, Cao H-M, Kong J-L, Xiong H-M, et al. ZnO-Based Nanoplatforms for Labeling and Treatment of Mouse Tumors without Detectable Toxic Side Effects. ACS nano. 2016;10:4294-300.

[43] Luo Z, Yuan X, Yu Y, Zhang Q, Leong DT, Lee JY, et al. From aggregation-induced emission of Au (I)–thiolate complexes to ultrabright Au (0)@ Au (I)–thiolate core–shell nanoclusters. J Am Chem Soc. 2012;134:16662-70.

[44] Gao Z, Lukyanov AN, Singhal A, Torchilin VP. Diacyllipid-polymer micelles as nanocarriers for poorly soluble anticancer drugs. Nano Lett. 2002;2:979-82.

[45] Mou F, Xu L, Ma H, Guan J, Chen D-r, Wang S. Facile preparation of magnetic γ-Fe 2 O 3/TiO 2 Janus hollow bowls with efficient visible-light photocatalytic activities by asymmetric shrinkage. Nanoscale. 2012;4:4650-7.

[46] Ye E, Regulacio MD, Bharathi MS, Pan H, Lin M, Bosman M, et al. An experimental and theoretical investigation of the anisotropic branching in gold nanocrosses. Nanoscale. 2016;8:543-52.

[47] Schmidbaur H. Ludwig Mond lecture. High-carat gold compounds. Chem Soc Rev. 1995;24:391-400.

[48] Ito H, Saito T, Oshima N, Kitamura N, Ishizaka S, Hinatsu Y, et al. Reversible mechanochromic luminescence of [(C6F5Au) 2 (μ-1, 4-Diisocyanobenzene)]. J Am Chem Soc. 2008;130:10044-5.

[49] Hong Y, Lam JW, Tang BZ. Aggregation-induced emission. Chem Soc Rev. 2011;40:5361-88.

[50] Ghosh SK, Pal T. Interparticle coupling effect on the surface plasmon resonance of gold nanoparticles: from theory to applications. Chem Rev 2007;107:4797-862.

[51] Liu D, Wang Z, Jiang X. Gold nanoparticles for the colorimetric and fluorescent detection of ions and small organic molecules. Nanoscale. 2011;3:1421-33.

[52] Md NS, Kim H-K, Park J-A, Chang Y, Kim T-J. Gold nanoparticles coated with Gd-chelate as a potential CT/MRI bimodal contrast agent. Bull Korean Chem Soc. 2010;31:1177-81.

[53] Alric C, Taleb J, Duc GL, Mandon C, Billotey C, Meur-Herland AL, et al. Gadolinium chelate coated gold nanoparticles as contrast agents for both X-ray computed tomography and magnetic resonance imaging. J Am Chem Soc. 2008;130:5908-15.

[54] Frangville C, Li Y, Billotey C, Talham DR, Taleb J, Roux P, et al. Assembly of double-hydrophilic block copolymers triggered by gadolinium ions: new colloidal MRI contrast agents. Nano lett. 2016; 16:4069–73

[55] Cheng Z, Thorek DL, Tsourkas A. Gadolinium‐Conjugated Dendrimer Nanoclusters as a Tumor‐Targeted T1 Magnetic Resonance Imaging Contrast Agent. Angew Chem-Int Edit. 2010;49:346-50.

[56] Yu M, Zhou C, Liu J, Hankins JD, Zheng J. Luminescent gold nanoparticles with pH-dependent membrane adsorption. J Am Chem Soc. 2011;133:11014-7.

[57] He C, Hu Y, Yin L, Tang C, Yin C. Effects of particle size and surface charge on cellular uptake and biodistribution of polymeric nanoparticles. Biomaterials. 2010;31:3657-66.

[58] Fröhlich E. The role of surface charge in cellular uptake and cytotoxicity of medical nanoparticles. Int J Nanomedicine. 2012;7:5577-91.

[59] Bu L, Xie J, Chen K, Huang J, Aguilar ZP, Wang A, et al. Assessment and comparison of magnetic nanoparticles as MRI contrast agents in a rodent model of human hepatocellular carcinoma. Contrast Media Mol Imaging. 2012;7:363-72.

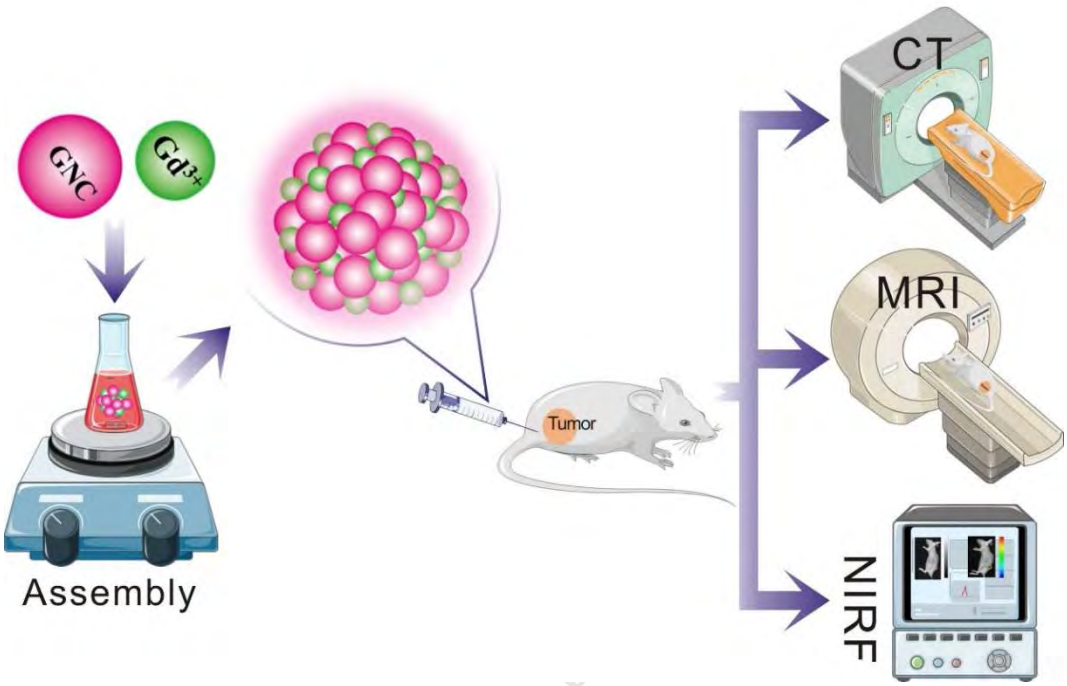

Scheme 1. Schematic illustration of gadolinium (Gd^{3+}) ions-mediated self-assembly of gold nanoclusters (GNCs) into monodisperse spherical nanoparticles (GNCNs) for multi-modality cancer diagnosis under mild conditions.

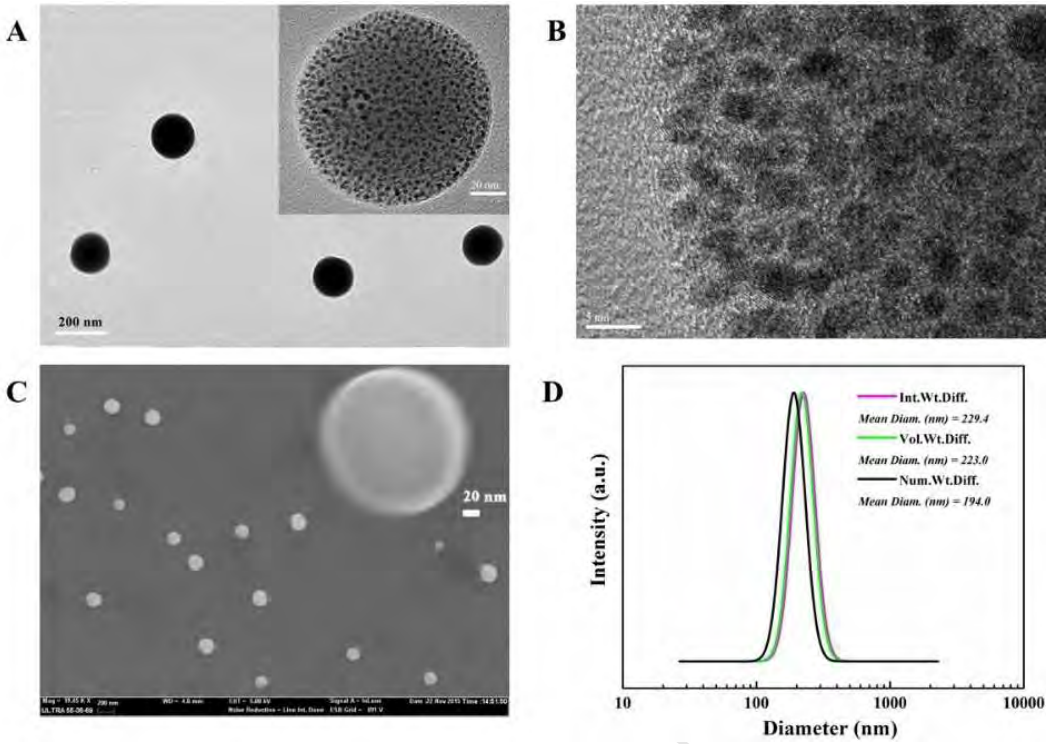

Fig. 1. Characterizations of the GNCNs. (A) TEM image of the GNCNs. (Inset) the amplified TEM image of the GNCNs. (B) HR-TEM image of the GNCNs. (C) SEM image of the GNCNs. (Inset) amplified SEM image of the GNCNs. (D) DLS curve shows the diameter distribution of the GNCNs.

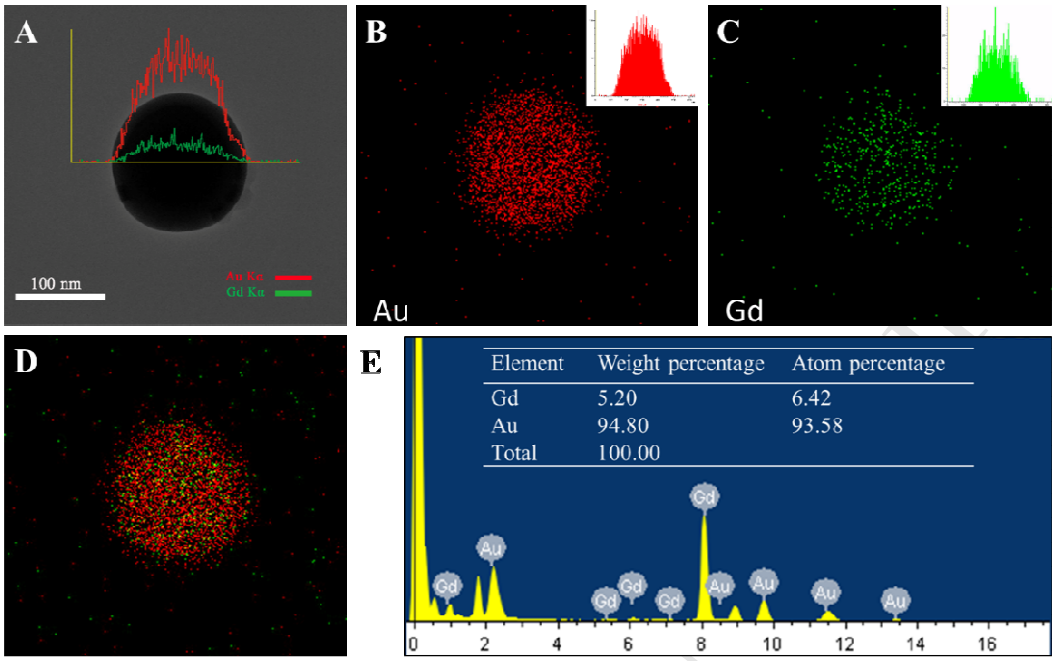

Fig. 2. (A) STEM image of a typical assembly (GNCNs). (B–C) The mapping EDX analysis of distribution of Au (B) and Gd (C) elements in a typical assembly in (A). The insets in (B) and (C) display the elemental line-scanning EDX analysis of Au (red curve) and Gd (green curve), respectively. (D) Shows the superimposing image of (B) and (C). (E) Shows the EDX spectrum analysis of the content of the Au and Gd elements of the typical assembly in (A).

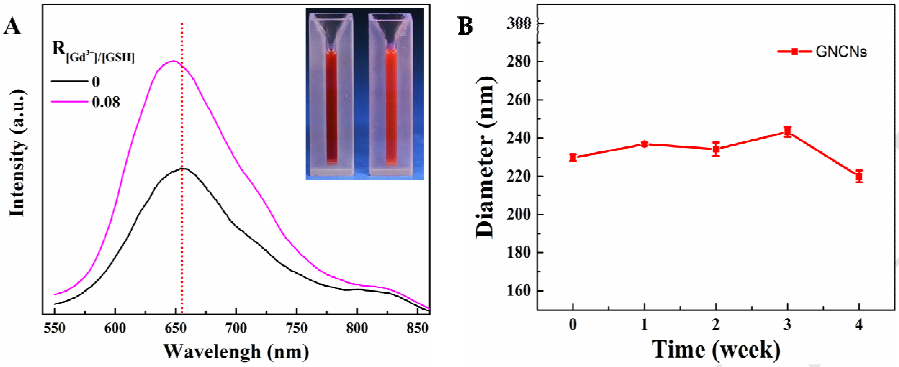

Fig. 3. (A) Fluorescence spectra of the GNCs and the GNCNs (λex = 520 nm). (Inset) Digital pictures of GNCs (left) and GNCNs (right) dissolved in aqueous solution under UV(365 nm) excitation. (B) Colloid stability test of GNCNs in aqueous solution (mean ± SD, n =3).

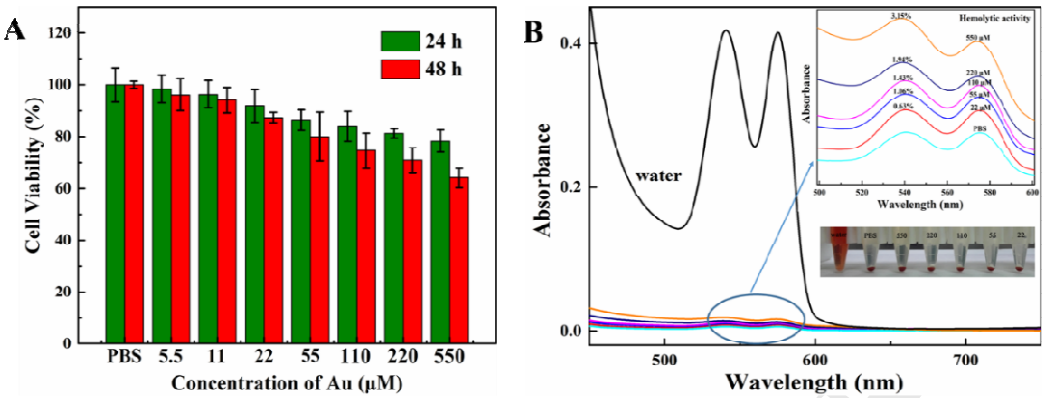

Fig. 4. (A) A549 cells viability measured by MTT assay after incubation with PBS (as control) and the GNCNs at different Au concentrations for 24 h and 48 h, respectively (mean ± SD, n =3). (B) Hemolytic activity of GNCNs at different Au concentrations. The bottom-right inset and the upper-right inset represent the photograph of HRBCs and the enlarged UV−Vis absorption of the supernatant after the blood incubation with water, PBS and GNCNs PBS solution at different Au concentrations for 2 h, respectively.

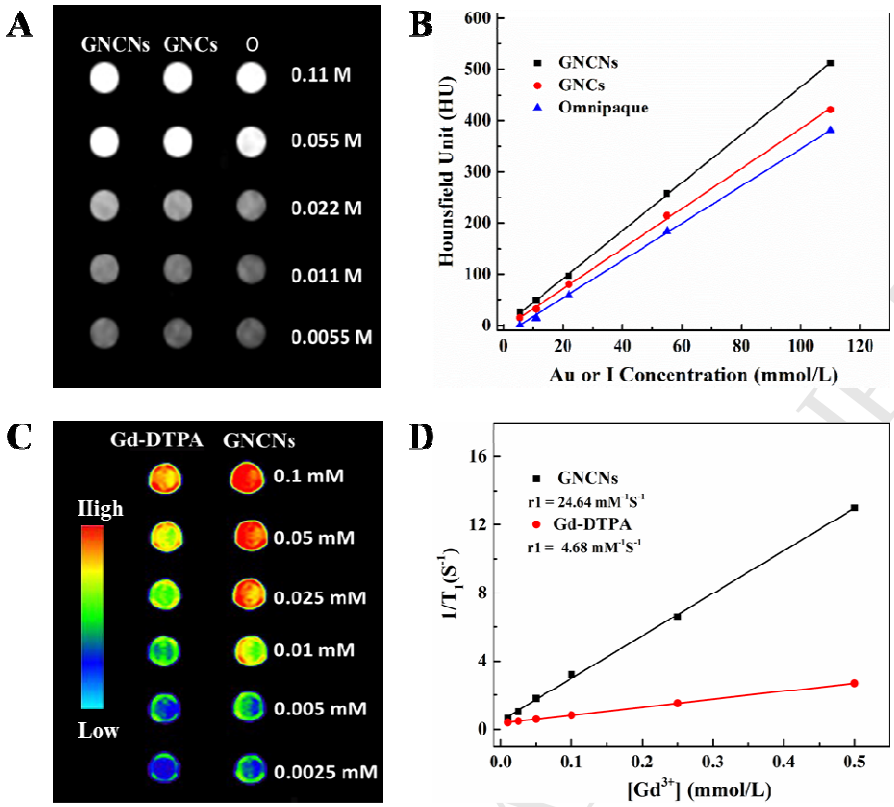

Fig. 5. X-ray attenuation property and T1 MR relaxometry of the GNCNs. (A) CT images and (B) X-ray attenuation intensity of GNCs, GNCNs and Omnipaque (O) at different Au or I concentrations, respectively. (C) T1-MR images of Gd-DTPA and GNCNs. (D) The linear fitting of the inverse T1 of Gd-DTPA and GNCNs as a function of Gd^{3+} ion concentration.

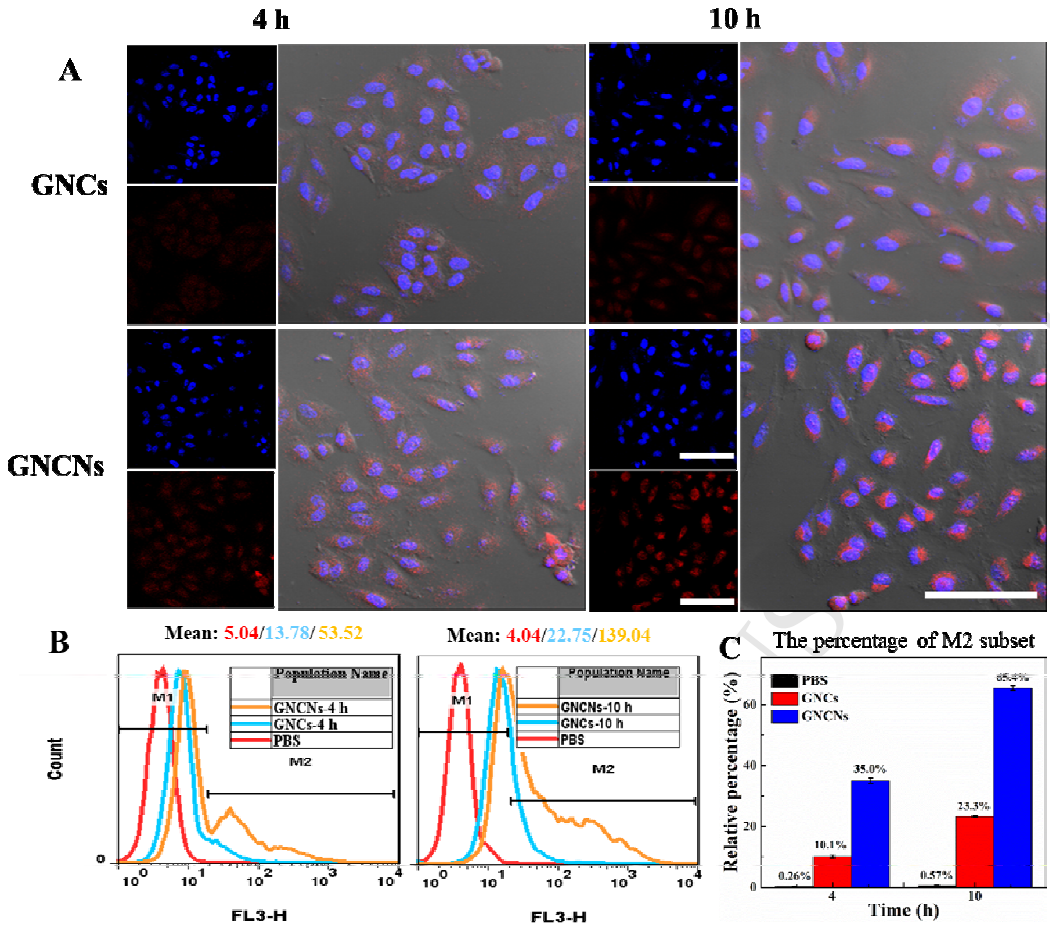

Fig. 6. Cellular uptake of GNCNs by A549 cells. (A) Confocal images of the A549 cells treated with GNCNs or GNCs for 4 and 10 h, respectively. Scale bar, 100 μm. (B) Flow cytometry analysis of the A549 cells incubated with GNCNs or GNCs for 4 and 10 h, respectively. Mean: mean fluorescence of M2 subset. (C) The population distribution histogram of A549 cells with GNCs or GNCNs (mean ± SD, n = 3).

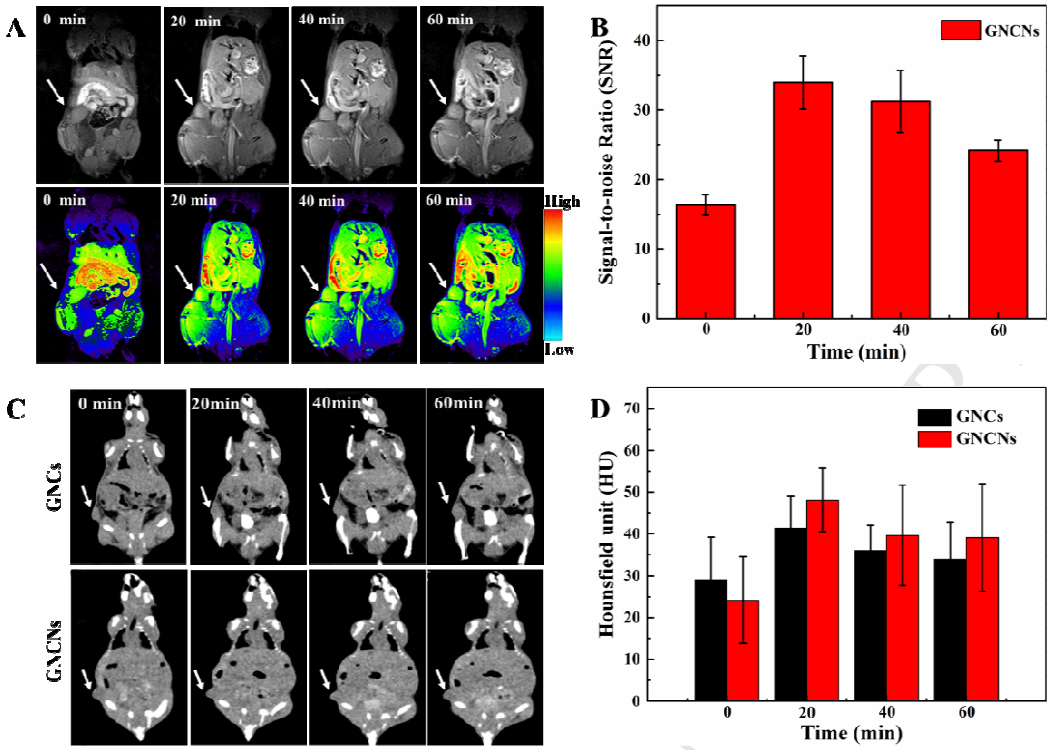

Fig. 7. *In vivo* X-ray CT/MR imaging. (A) *In vivo* T1-weighted MR images of A549 tumor-bearing mice post intravenous injection of GNCNs at different time points. (B) T1 signal to noise ratio around the tumors of (A). (C) CT images of A549 tumors-bearing mice post intravenous injection of GNCs or GNCNs at different time points. (D) CT values around the tumors of (C). The arrows point indicate the location of the tumor area (mean ± SD, n =3).

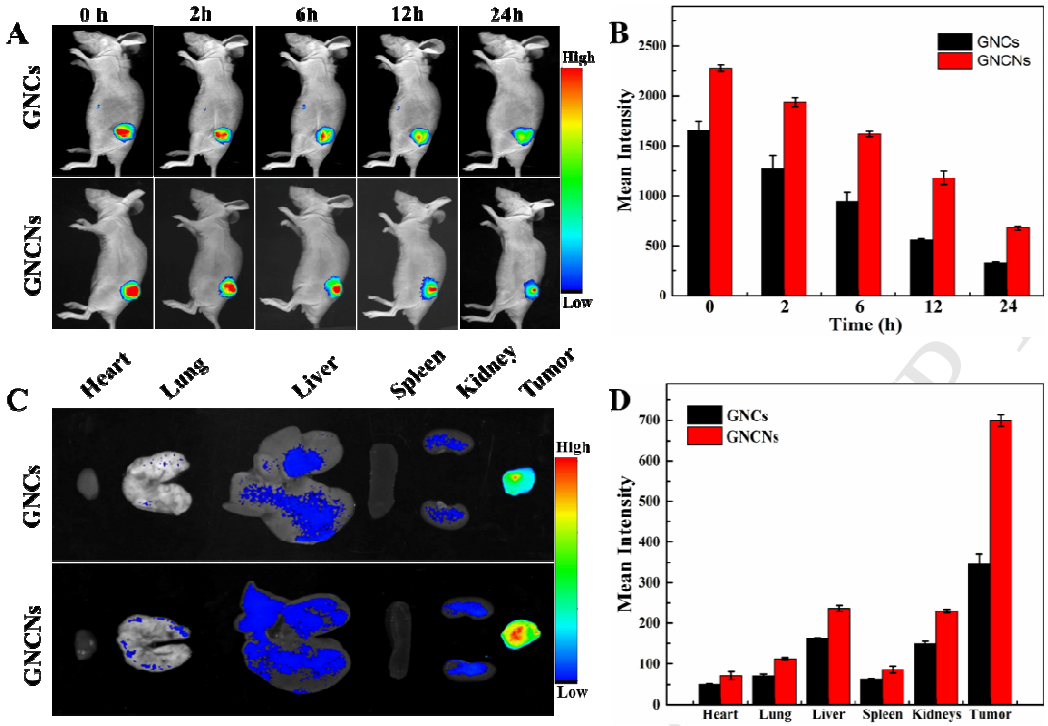

Fig. 8. *In vivo* NIRF imaging and biodistribution of the A549 tumor-bearing mice post intratumoral injection of GNCNs or GNCs. (A) *In vivo* time-dependent NIRF imaging of A549 tumor-bearing nude mice. (B) The average fluorescence signal intensities around the tumors of (A) (mean ± SD, n =3). (C) *In vitro* biodistribution of the extracted main organs and tumors at 24 h post intratumoral injection of GNCNs or GNCs. (D) The average fluorescence intensities of (C) (3 mice/group).